Supplementary Material

Uncovering the Effect of Lattice Strain and Atomic-Scale Cavities Deficiency on Efficient Oxygen Reduction of PdW Bimetallene

Jigang Wang[a,*], Xia Zhou[a], Yinggang Sun[a], Xiuhui Bai[c,*], Lancheng Zhao[a], Siqi Wang[a], Likai Wang[a,*], Huan Liu[b,*], Zhongfang Li[a]

[a] School of Chemistry and Chemical Engineering, Shandong University of Technology, Zibo, Shandong 255049, China

[b] College of Chemistry and Materials Science, Anhui Normal University, Wuhu 241002, China

[c] College of Chemical Engineering and Materials Science, Tianjin University of Science and Technology, Tianjin, 300457, China

* Corresponding author, E-mail: jgwang2008@sdut.edu.cn (J. W); xhuibai@163.com (X. B); lkwangchem@sdut.edu.cn (L. W); huanliu@ahnu.edu.cn (H. L)

METHODS

Material. Palladium(II) acetylacetonate ($Pd(acac)_2$), Sodium tetrachloropalladate (II) (Na_2PdCl_4), Sodium bromide (NaBr), molybdenum carbonyl ($Mo(CO)_6$), Oleylamine, Cyclohexane, L-Ascorbic acid ($C_6H_8O_6$), Ethylene glycol ($C_2H_6O_2$), Potassium hydroxide (KOH), Diethylenetriamine ($C_4H_{13}N_3$), N, N-dimethylformamide (DMF), Diethylenetriamine (DETA) and Nafion (5%) were purchased from Sigma-Aldrich. Ethanol (99.9%) was purchased from Damao. O_2 (purity 99.995%), Ar (purity 99.99%), N_2 (purity 99.99%) and H_2 (purity 99.999%) were obtained from Zibo Baiyan Gases. DI water was obtained from a Barnstead Nanopure water purification system (18.3 MΩ cm). All materials were used without further purification.

Synthesis of samples. First, $W(CO)_6$ (10 mg) and $C_6H_8O_6$ (20 mg) were dissolved in Oleylamine (5 ml) at 70℃, and then cooled to room temperature to obtain solution 1. Then $Pd(acac)_2$ (10 mg) was added to solution 1, and a uniform solution was obtained by ultrasonic treatment. The solution was sealed and reacted at 80°C for different times (10, 12, 14, 16 h). After centrifugation and washing, the product was obtained, which was PdW. d-PdW was obtained by dispersing PdW into cyclohexane, adding 10 ul 10 mM NaBr solution, and reacting at 45℃ for 10, 12, 14 h.

For p-Pd, Na_2PdCl_4 is first dissolved in DMF and $C_2H_6O_2$ solution, then KOH is added and ultrasound to obtain a uniform solution, followed by dropwise addition of DETA. The final product is obtained by oil bath at 150℃ for 1 h, followed by centrifugation and ethanol washing, and labeled as p-Pd.[1]

Characterization. The morphology, crystal structure, valence state, and coordination environment of the material were characterized by scanning electron microscopy (SEM)/high-resolution transmission electron microscopy (HRTEM), X-ray diffraction (XRD), X-ray photoelectron spectroscopy (XPS), and X-ray absorption spectroscopy (XAS), respectively. Inductively coupled plasma atomic emission spectrometer (ICP-AES) is used to analyze the content of different elements.

Theoretical Calculations. Density functional theory (DFT) calculations were conducted utilizing the Vienna Ab Initio Simulation Package (VASP).[2] The electronic exchange and correlation effects were modeled using the Perdew–Burke–

Ernzerhof (PBE) function in combination with the generalized gradient approximation (GGA). Three models with three stoichiometric layers of Pd (111), PdW (111), and d-PdW (111) are used for calculation, respectively. The self-consistent field (SCF) tolerance, k-point, the maximum displacement and the energy cut-off were set to 1×10^{-6} eV, 3 × 3 ×3, 0.001 Å, and 571.4 eV, respectively. For all the models, the 2 × 2 supercell was built with vacuum layer of 15 Å and two bottom layers were fixed.

Electrochemical Measurements. ORR test was conducted in O_2-saturated 1M KOH using a WaveDriver 20 bipotentiostat, in which glassy carbon rotating disk electrode (RDE, 5 mm in diameter) or rotating ring-disk electrode (RRDE, 5 mm in inner diameter and 8.5 mm in outer diameter), carbon rod and silver chloride electrode were used as working, counter and reference electrode, respectively. The loaded catalysts on the electrode were ~0.2 mg cm^{-2}. All potentials were converted to the reversible hydrogen electrode (RHE) reference scale using: $E_{RHE} = E_{Ag/AgCl} + 0.059*pH + 0.197$. Cyclic voltammetry (CV) tests with a sweep rate of 50 mV s^{-1} were conducted in O_2- or N_2-saturated electrolyte. The ORR activity measurement was carried out in O_2-saturated electrolyte with a sweep rate of 10 mV s^{-1}, and the RDE rotation speed was 1600 rpm without IR compensation.

The electrochemical surface area (ECSA) of Pd-based samples was determined using the equation ECSA = Q / (m·C), where Q represents the coulomb charge (mC) derived from integrating the PdO reduction peak area, and C denotes the theoretical charge for reducing a monolayer of PdO (405 μC cm^{-2}). For Pt/C, Q corresponds to the charge in the hydrogen adsorption/desorption region, m is the Pt loading mass, and C is the hydrogen monolayer adsorption charge on Pt (210 μC cm^{-2}).[3]

The apparent electron transfer number was calculated by the Koutecky-Levich (K–L) equation at various potentials ($1/j = 1/j_K + 1/j_L = 1/nFkC_0 + 1/Bw^{1/2}$), where j is the measured current density, j_K and j_L are the kinetic and limiting current densities, respectively. The yield of H_2O_2 and the electron transfer number (n) were calculated from the RRDE measurement: $H_2O_2\% = 200*I_r/(I_dN+I_r)$, where N is the current collection efficiency of the RRDE (0.37), I_r is the ring current and I_d is the disk current.[4]

Zn-Air Battery Measurements. The liquid Zn-air batteries were carried out in a self-made device, with Zn foil as the anode, carbon cloth loaded with catalyst (1.0 mg cm^{-1}) as the cathode, and 6 M KOH containing 0.2 M zinc acetate as the electrolyte. The polarization curves and charging-discharge stability of the batteries were tested at the electrochemical workstation (Shanghai Chenhua, China) and Neware CT-4008 system.

For flexible solid-state Zn-air batteries, Zn foil serves as the anode, PVA gel polymer as solid electrolyte, and carbon cloth loaded with the catalyst (1.0 mg cm^{-1}) as the cathode. To prepare the PVA gel polymer, 1.6 g of Polyvinyl Alcohol (PVA) was dissolved in 18 mL of DI water at 90℃. Then, 2.0 g of KOH and 8.8 g of zinc acetate were added to the above solution, stirred for 20 minutes, and the mixed solution was frozen in the refrigerator.

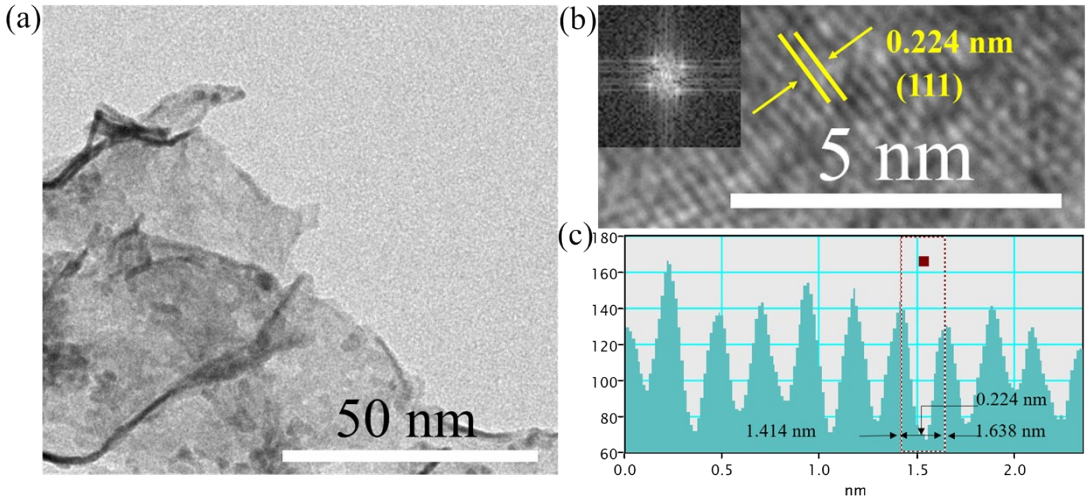

Fig. S1. (a) TEM, (b) HR-TEM image and FFT pattern (inset in (b)) and (c) lattice spacing diagram of p-Pd.

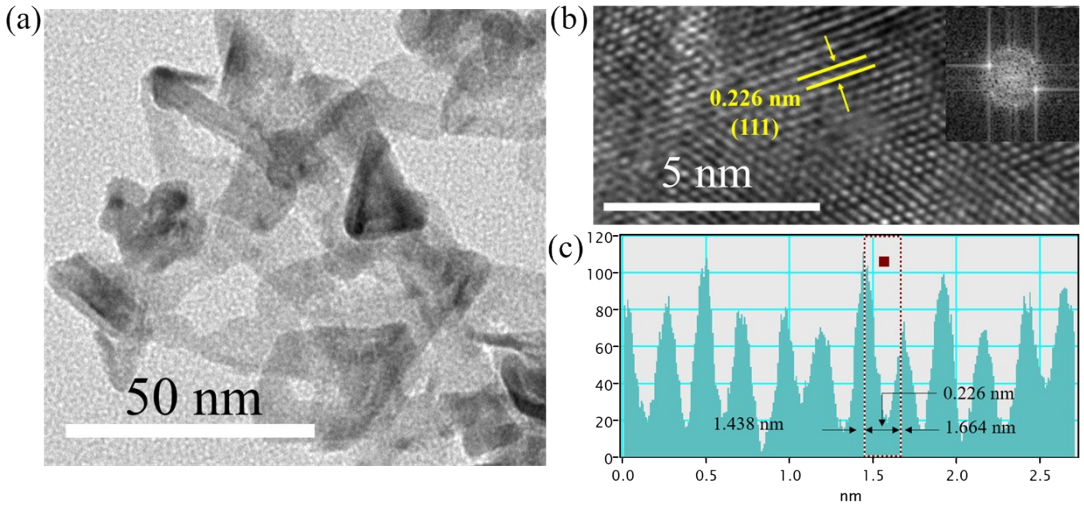

Fig. S2. (a) TEM, (b) HR-TEM image and FFT pattern (inset in (b)) and (c) lattice spacing diagram of PdW.

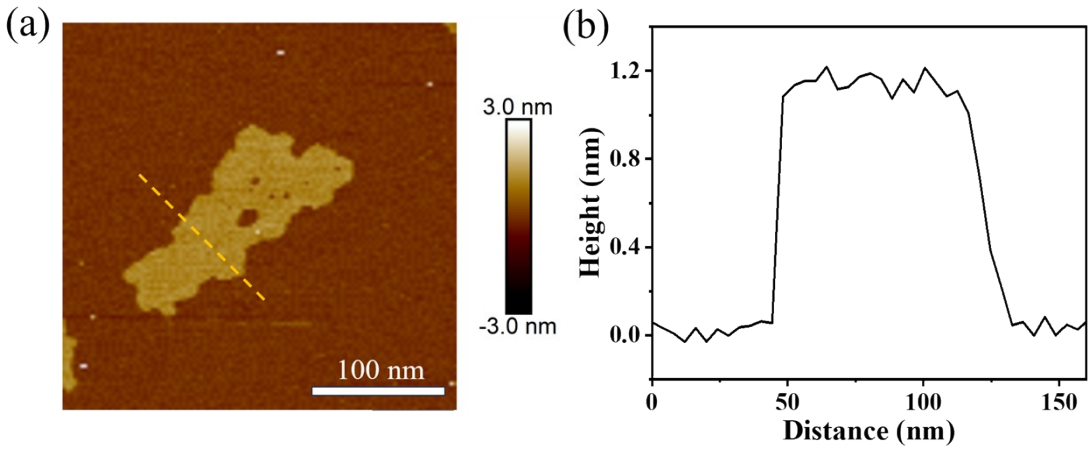

Fig. S3. (a) A typical AFM image of d-PdW. (b) Section analysis of d-PdW along the dashed line in (a).

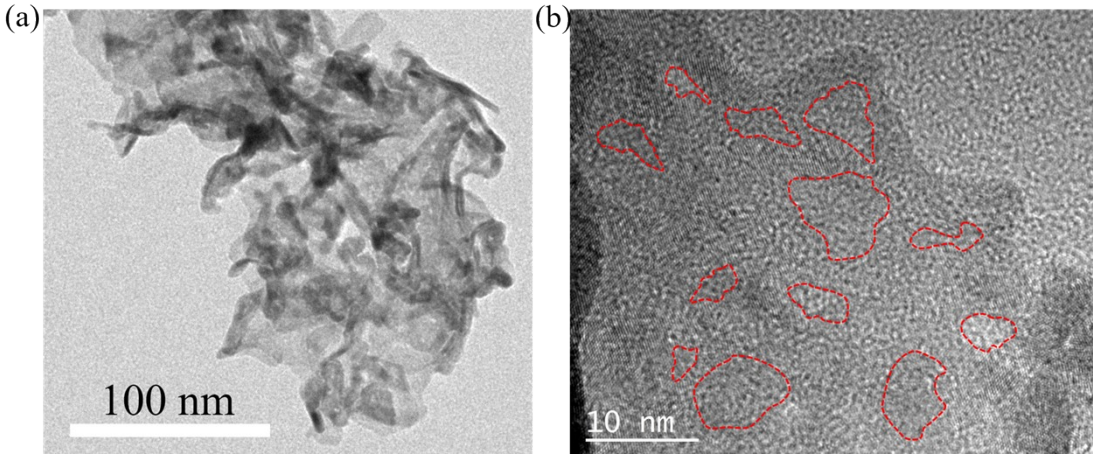

Fig. S4. (a) TEM, (b) HR-TEM images of d-PdW.

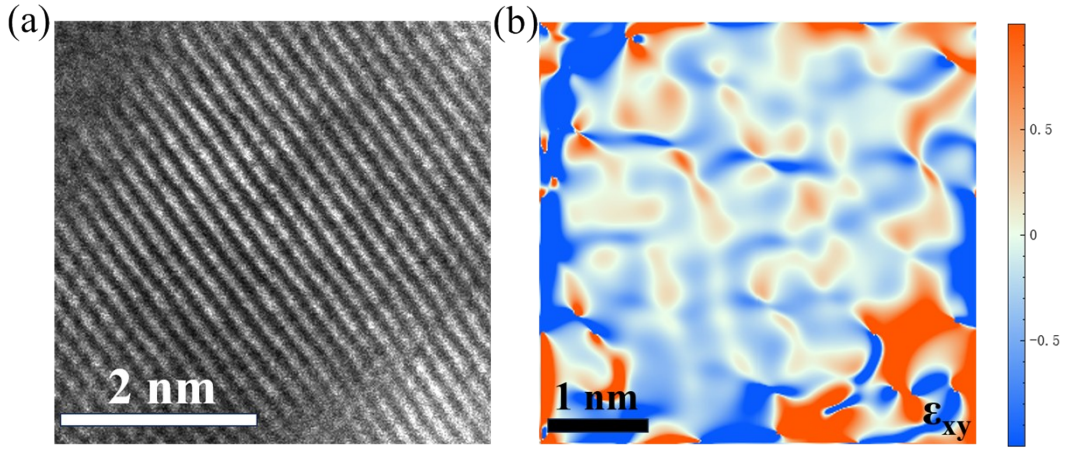

Fig. S5. (a) HRTEM images of d-PdW. (b) The color maps of GPA of the images (a) along ε_{xy}.

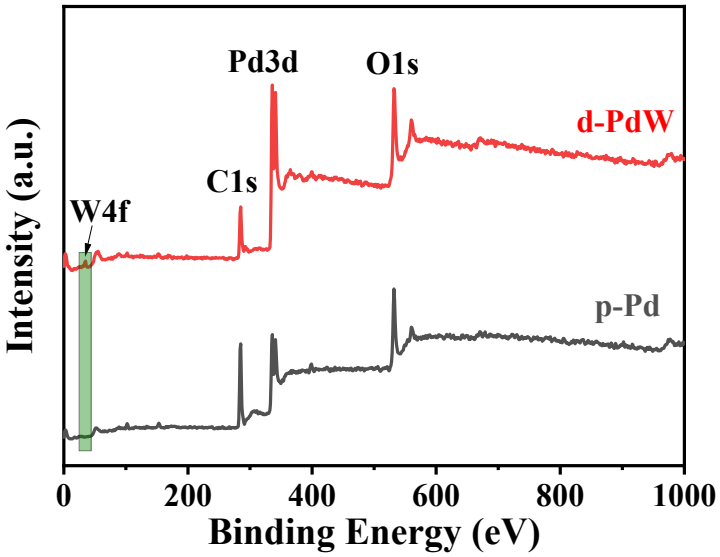

Fig. S6. XPS survey spectra of p-Pd and d-PdW.

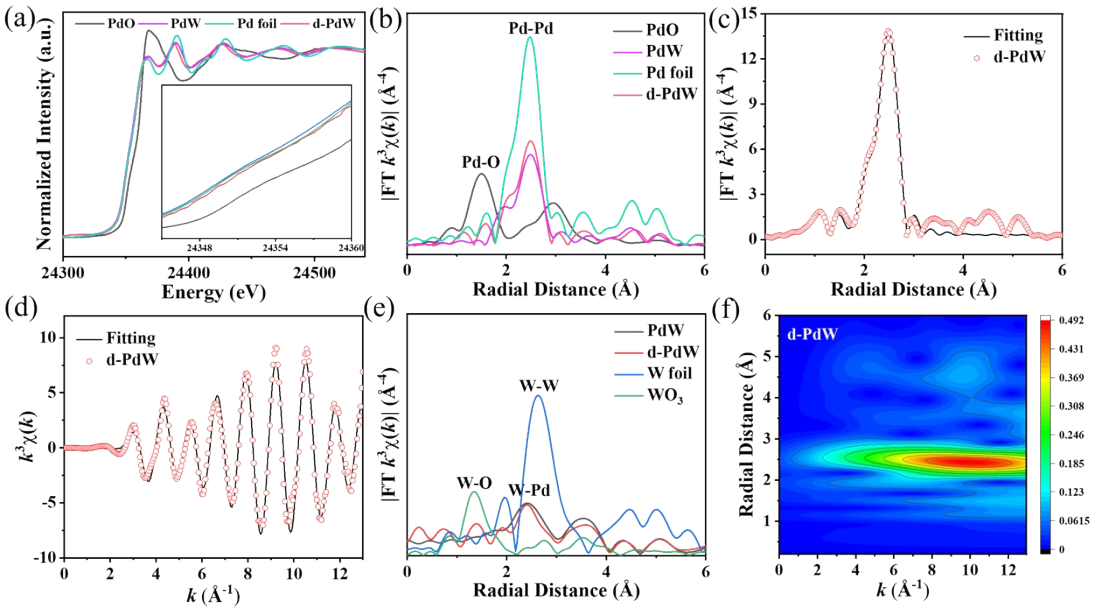

Fig. S7. Pd K-edge XAFS characterizations of various samples: (a) XANES spectra, (b) EXAFS spectra, (c, d) corresponding EXAFS fitting and (f) WT profiles. W L_3-edge XAFS characterizations of various samples: (e) EXAFS spectra.

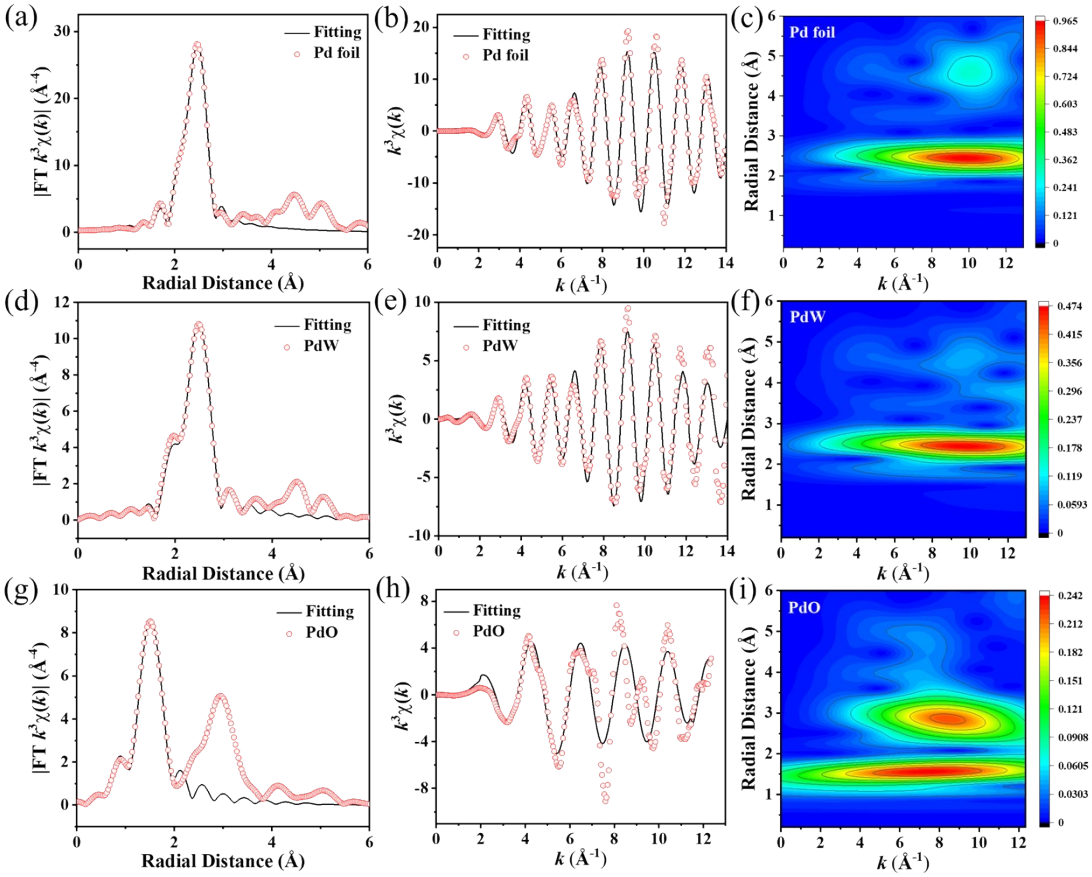

Fig. S8. EXAFS fitting curves in the (a,d,g) R and (b,e,h) k space of the various samples. (c,f,i) The corresponding Wavelet transforms of the k^3-weighted EXAFS signals.

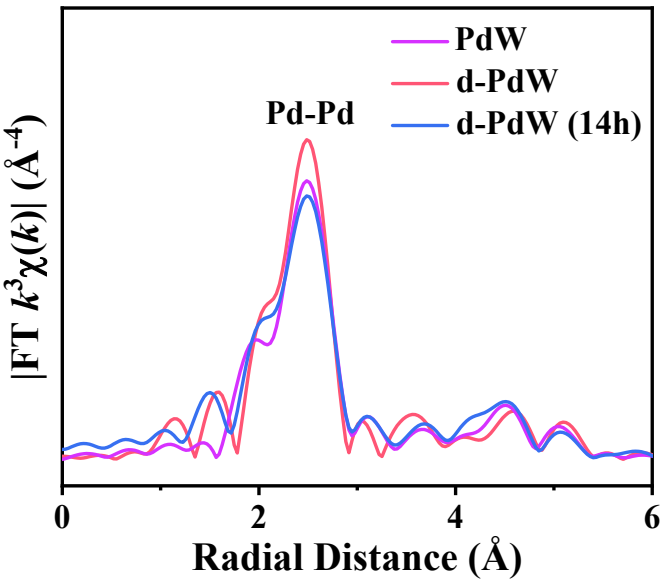

Fig. S9. EXAFS analysis of Pd K edge.

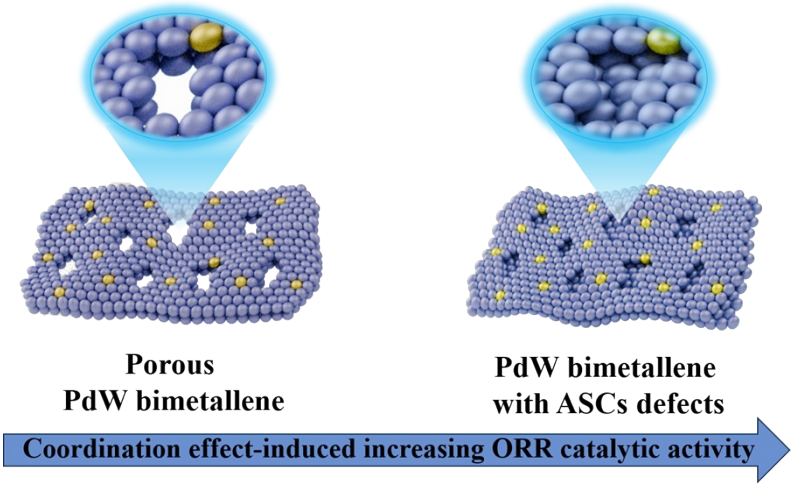

Fig. S10. Schematic illustration of local coordination environment around different types of defects.

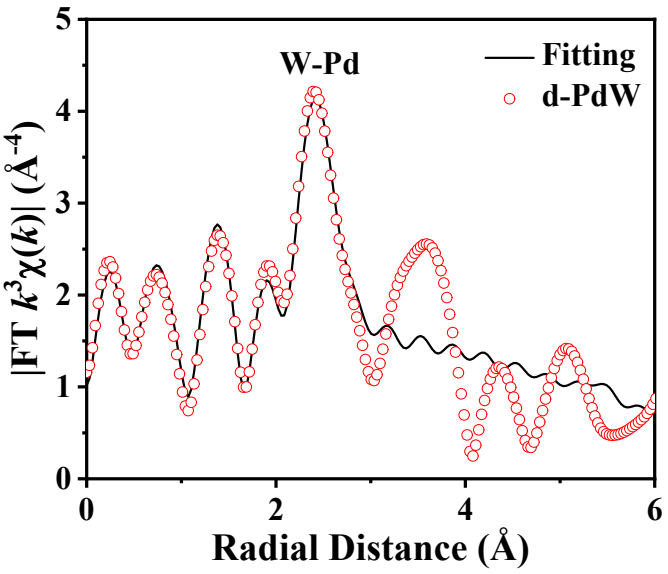

Fig. S11. W L_3-edge EXAFS fitting of d-PdW.

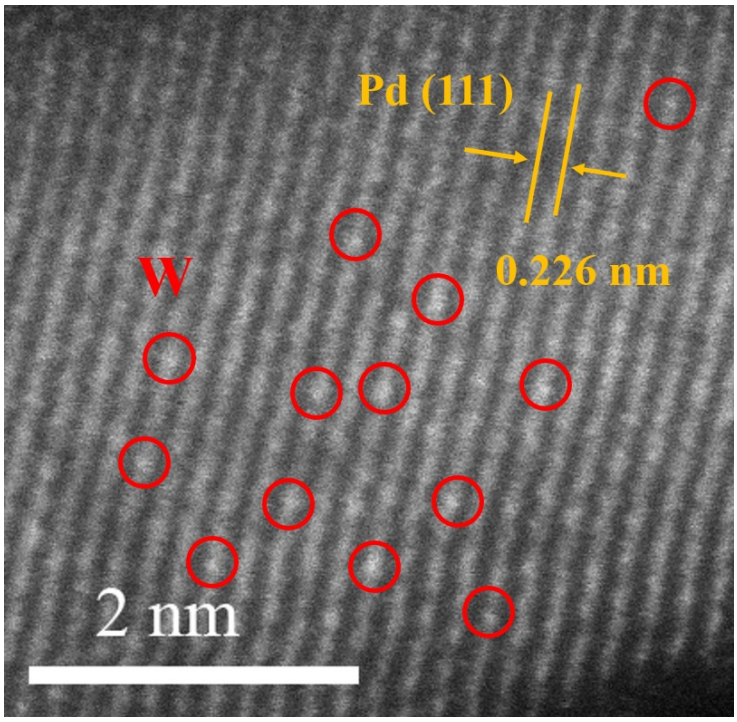

Fig. S12. The aberration-corrected high-angle annular dark-field scanning transmission microscopy (AC-HAADF-STEM) image of d-PdW.

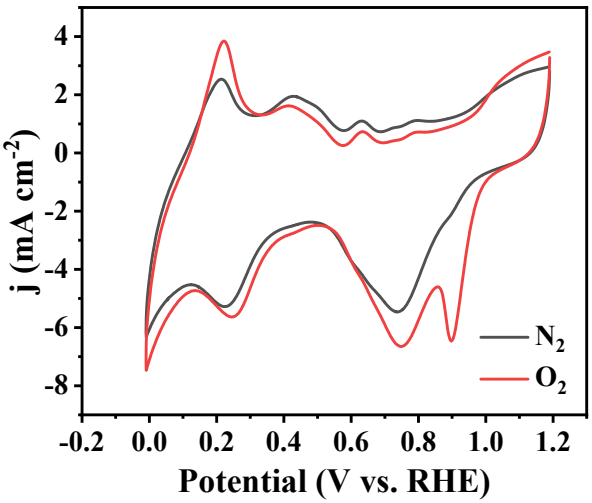

Fig. S13. The cyclic voltammetric (CV) curves of d-PdW in N_2- and O_2- saturated 0.1 M KOH solution.

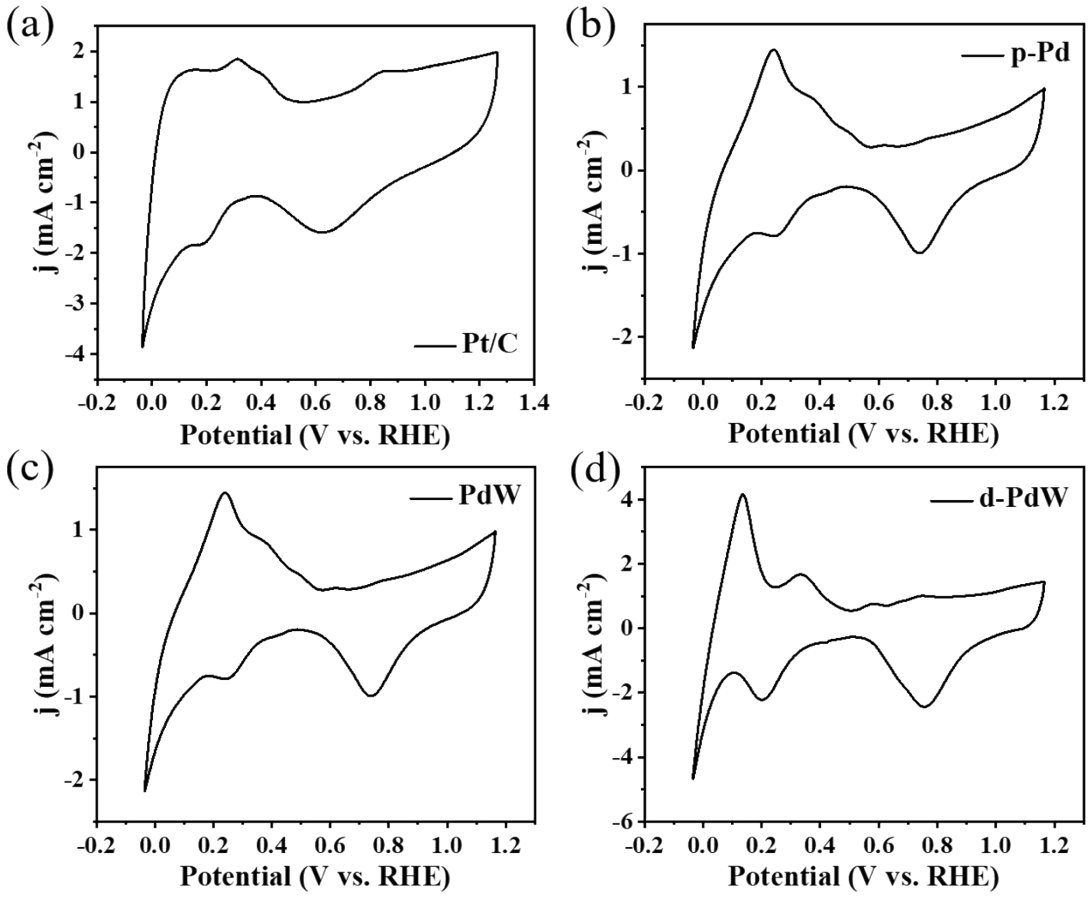

Fig. S14. The cyclic voltammetric (CV) curves in 0.1 M KOH solution. (a) Pt/C, (b) p-Pd, (c) PdW and d-PdW.

The electrochemically active surface area (ECSA) of Pt/C, p-Pd, PdW, and d-PdW was around 17.6, 14.3, 16.5, and 17.8 $m^2 \cdot g^{-1}$, respectively, which were calculated from the typical CV curves (Fig. S14), indicating that d-PdW can exposes more active sites, thereby improving ORR performance.

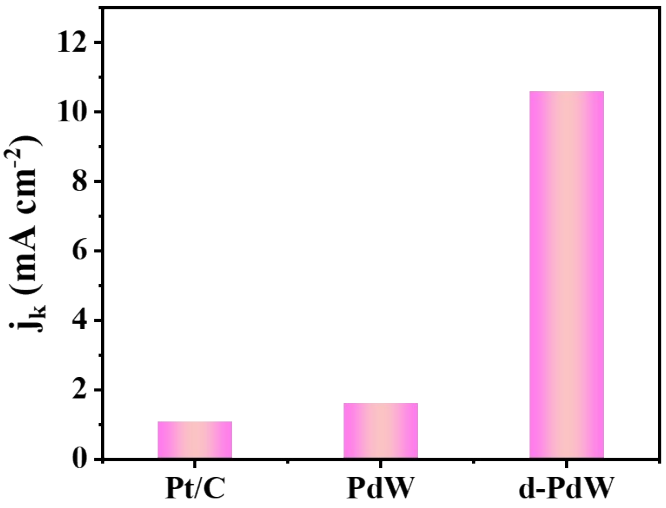

Fig. S15. The comparison of kinetic current density (j_k) at 0.9 V vs. RHE.

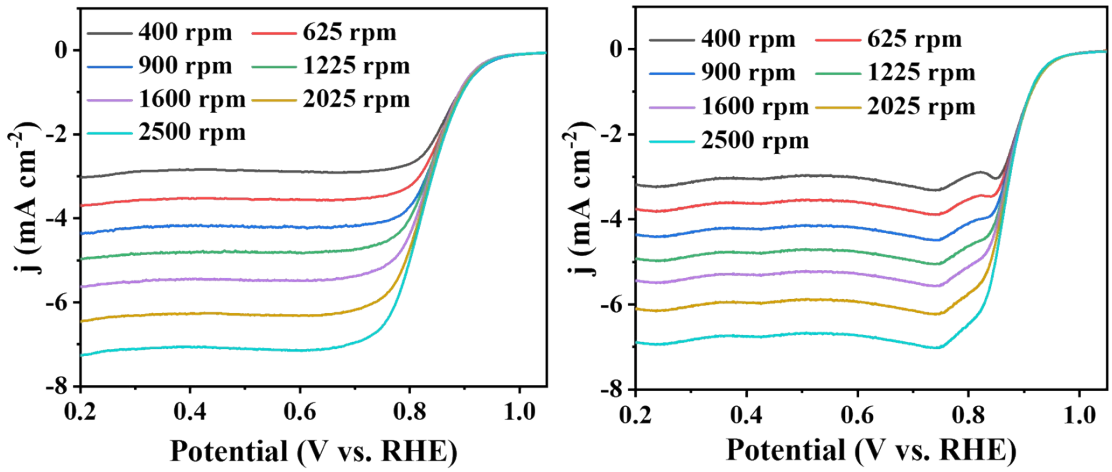

Fig. S16. ORR LSV curves on various rotating rates of Pt/C (a) and PdW (b).

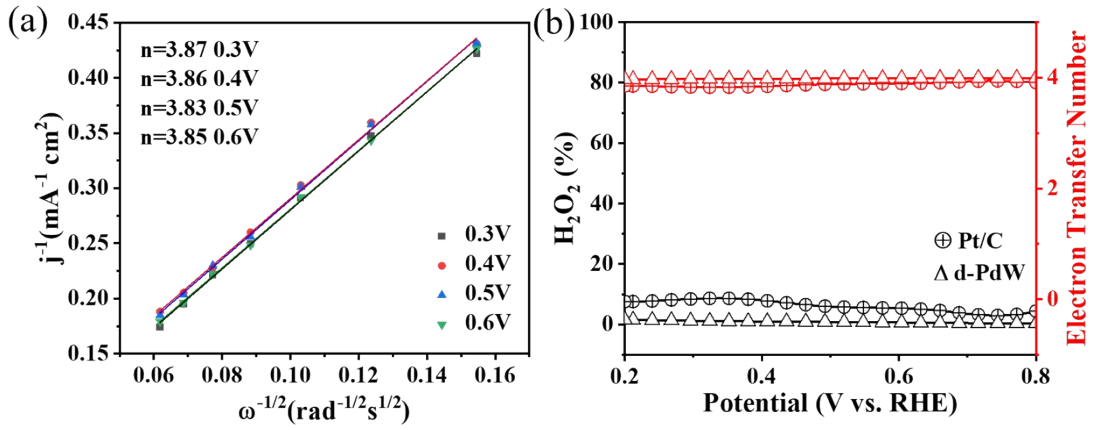

Fig. S17. (a) corresponding K-L curves of d-PdW. (b) electron transfer number and H_2O_2 yield of d-PdW and commercial Pt/C.

Based on the K-L equation, the average electron transfer number for d-PdW was calculated to be 3.84, indicating a dominant 4-electron oxygen reduction pathway (Fig. S17).

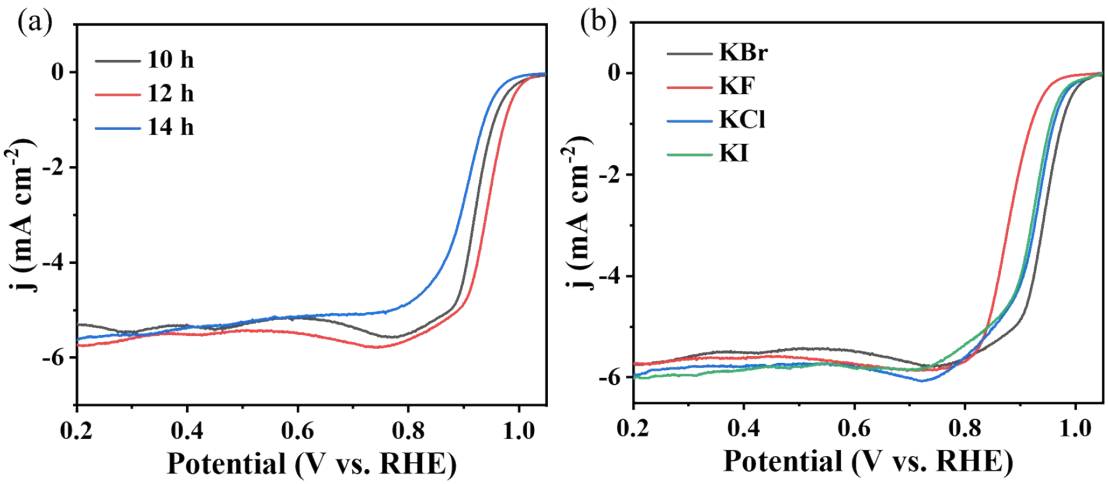

Fig. S18. LSV curves for ORR of d-PdW with different etching times with KBr (a) and different halogens (b).

As shown in Fig. S18, with the increase of time, the performance actually decreases, which may be due to the prolonged etching time causing the original ASCs defects to transform into porous defects (Fig. S9 and S10), which reduces the coordination number of Pd.

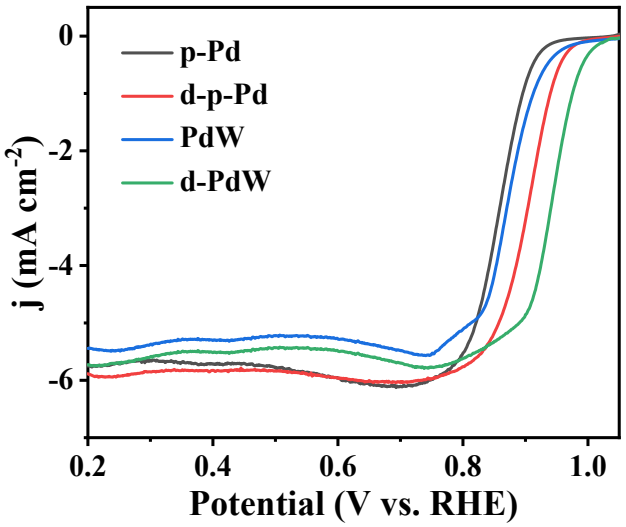

Fig. S19. LSV curves for ORR of p-Pd, d-p-Pd, PdW and d-PdW.

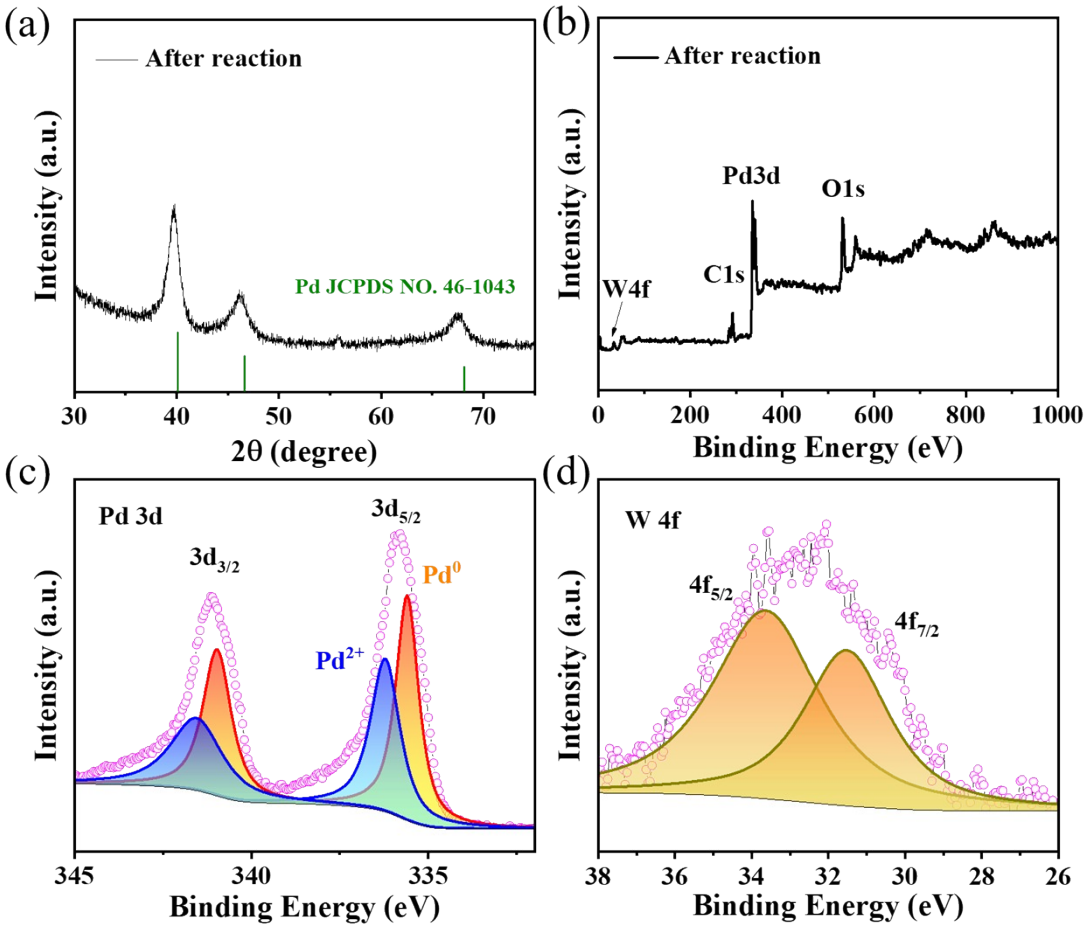

Fig. S20. XRD (a) and XPS (b-d) patterns of d-PdW after reaction.

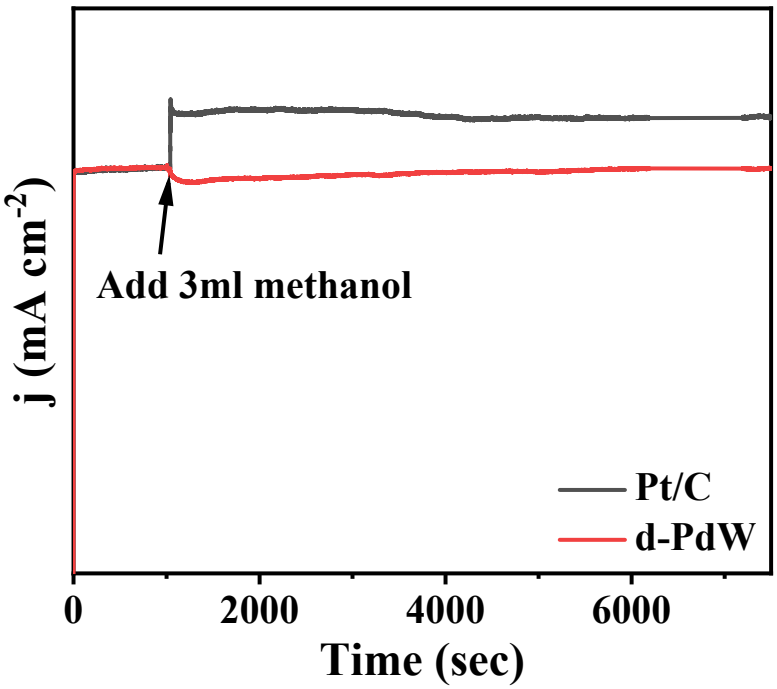

Fig. S21. Current density−time chronoamperometric response of d-PdW and Pt/C by adding 3 mL of methanol after about 1000 s.

In O_2-saturated 0.1 M KOH electrolyte, methanol-resistance durability was evaluated by introducing 3mL methanol after 1000 s. As shown in Fig. S21, d-PdW exhibits no noticeable disturbance of the current density, whereas Pt/C exhibits a dramatic methanol oxidation current signal.

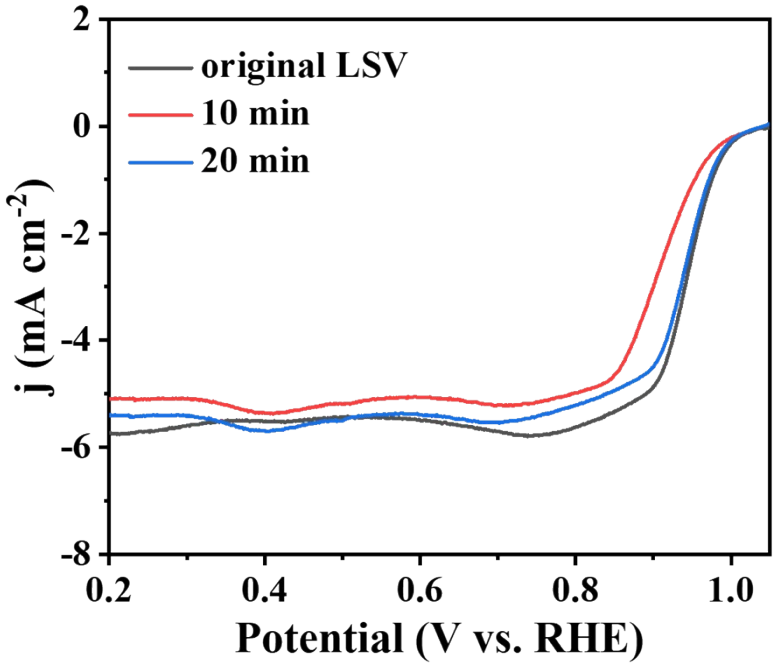

Fig. S22. LSV curves at different times after replacing the electrolyte containing methanol with a new 1 M KOH electrolyte.

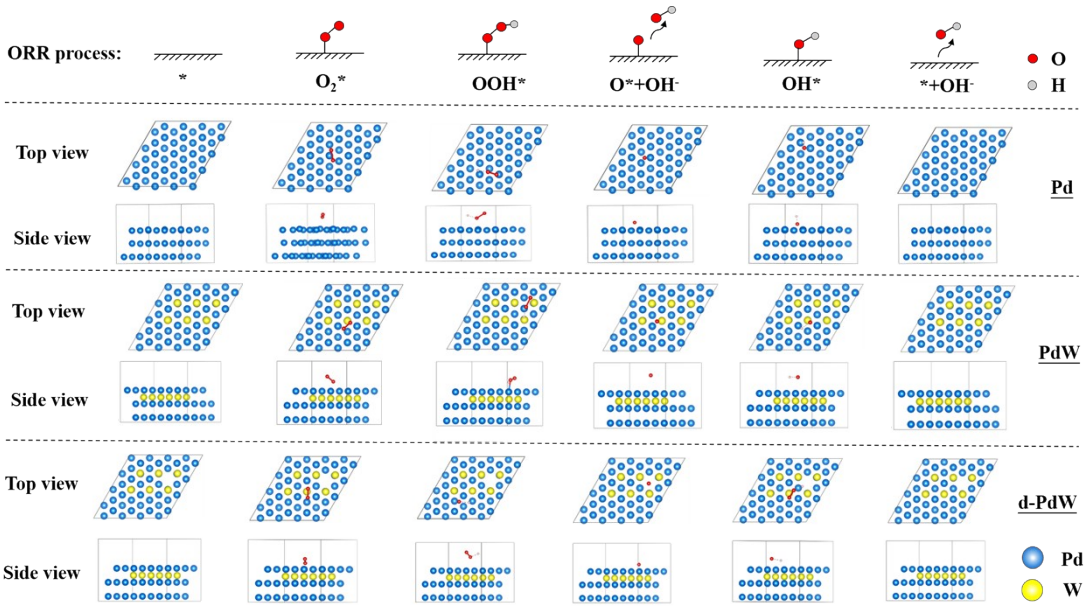

Fig. S23. DFT optimized structures for reaction intermediates on Pd (111), PdW (111) and d-PdW (111).

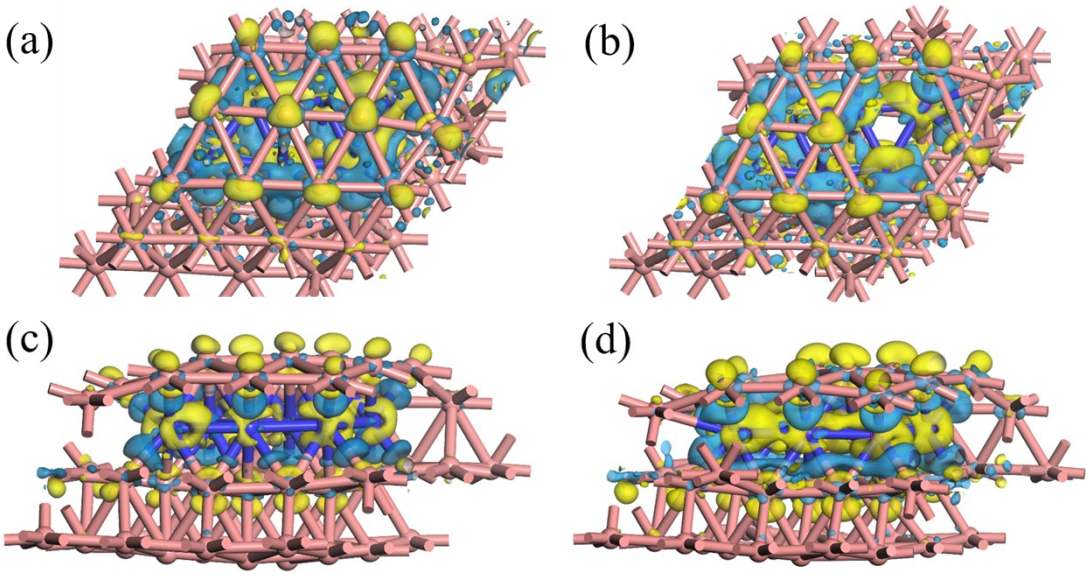

Fig. S24. The electron density difference maps for (a,c) PdW and (b,d) d-PdW (yellow and blue regions represent charge accumulation and depletion, respectively).

According to electron density difference (EDD), d-PdW exhibits a more electron-rich environment compared to PdW (Fig. S24). Due to the difference in electronegativity, electrons are transferred from W to Pd, increasing the electron density around Pd. After the introduction of defects, Pd atoms exhibits a more electron-rich environment, indicating a redistribution of electrons at the nearby Pd center, which reduces the adsorption of intermediates.

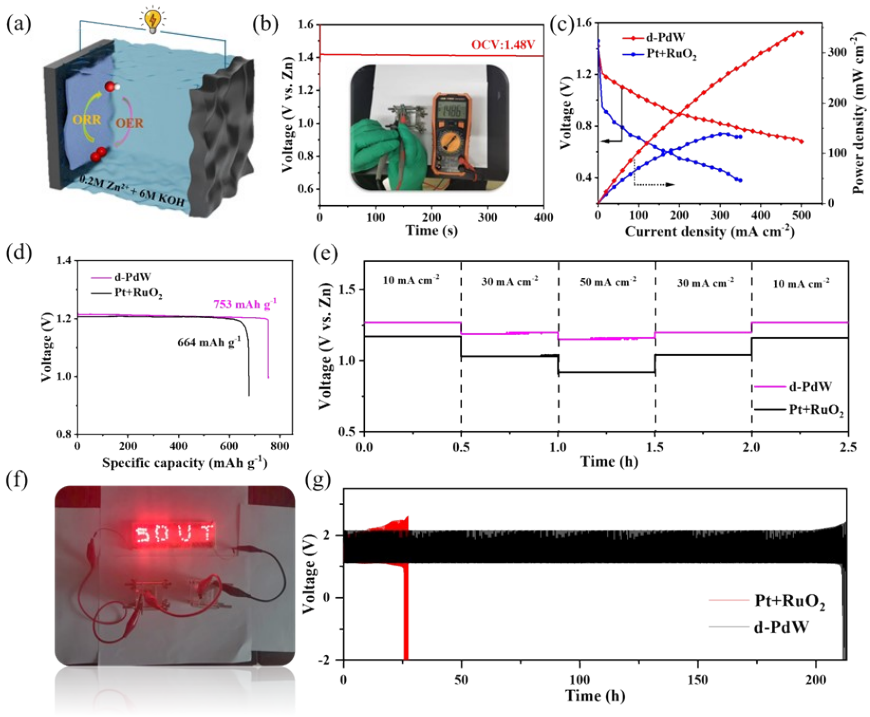

Fig. S25. (a) Schematic diagram of a Zn-air battery. (b) The open-circuit plots. (c) Polarization and corresponding power density curves. (d) discharge capacity at a current density of 10 mA cm^{-2}. (e) Discharge curves of two Zn–air batteries at current densities of 10, 30 and 50 mA cm^{-2}. (f) LED panel (2-5 V) powered by two series-connected Zn-air batteries. (g) Charge–discharge profiles of two Zn–air batteries at a current density of 10 mA cm^{-2}.

Inspired by the exceptional ORR activity for d-PdW, the liquid ZABs with d-PdW as the cathode catalyst (denoted as LZAB@d-PdW) were assembled (Fig. S25a). For comparison, a reference ZAB was also assembled by replacing d-PdW with commercial Pt/C+RuO_2 (denoted as LZAB@Pt/C+RuO_2). As shown in Fig. S25b, LZAB@d-PdW displays a stable open-circuit voltage (OCV) of 1.48 V and a maximum power density of 343 mW cm^{-2}, which are better than those of LZAB@Pt/C+RuO_2 catalyst (139 mW cm^{-2}, Fig. S25c). Furthermore, the discharge specific capacity of LZAB@d-PdW is 753 mAh g_{Zn}^{-1} at the current density of 10 mA cm^{-2}, which is more outstanding than that of LZAB@Pt/C+RuO_2 (664 mAh g_{Zn}^{-1}) (Fig. S25d). In addition, LZAB@d-PdW has higher discharging plateaus at different current densities (10 to 50 mA cm^{-2}) than that of the LZAB@Pt/C+RuO_2 (Fig. S25e). Such double series-wound

LZAB@d-PdW can drive a red LED array (2-5 V), which suggesting promising application in energy storage (Fig. S25f). As shown in Fig. S25g, the galvanostatic charge–discharge tests at the current density of 10 mA cm^{-2} illustrate that the LZAB@d-PdW displays no obvious changes in discharging and charging voltages after 1227 cycles (208 h).

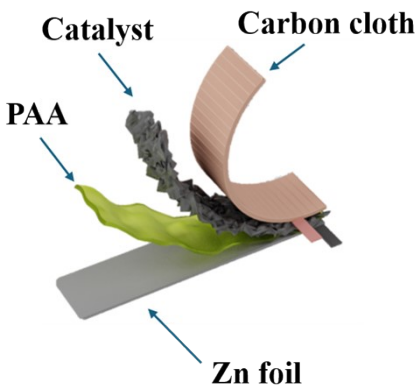

Fig. S26. Schematic diagram of a flexible solid-state Zn-air battery.

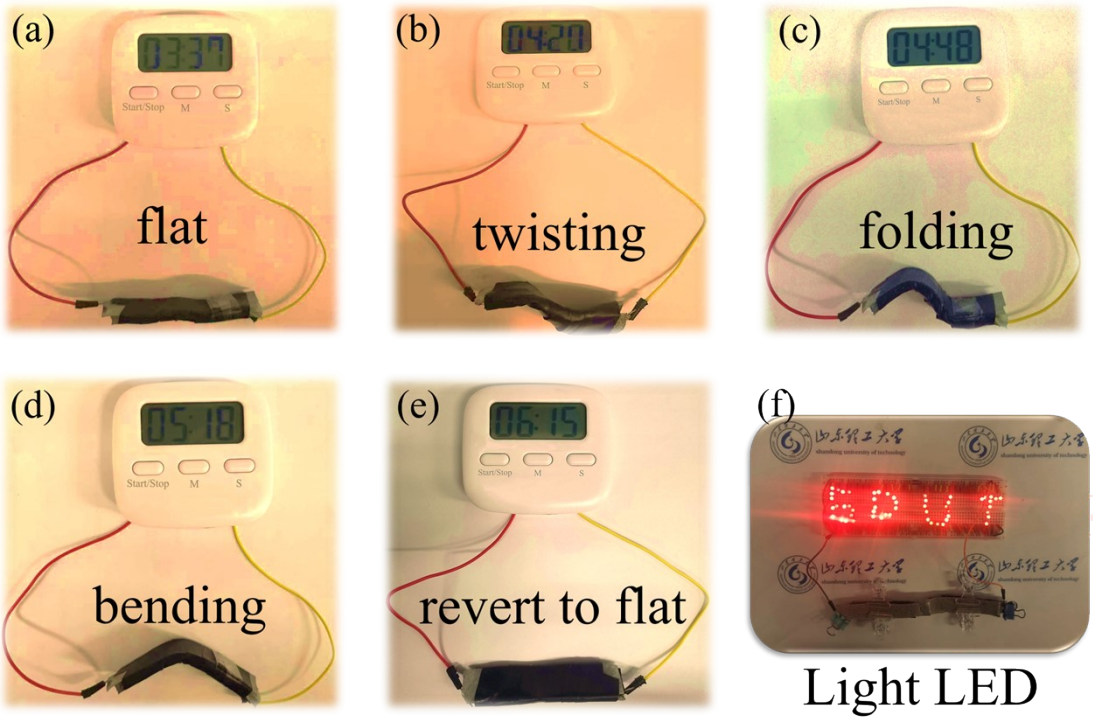

Fig. S27. (a-e) photos of a timer powered by FZAB@d-PdW upon different deformation conditions. (f) photo of a LED panel powered by two FZAB@d-PdW connected in series.

Table S1. W content (wt%) of the samples determined by ICP-OES.

sample	W (wt%)
PdW	2.1
d-PdW	2.0

Table S2. EXAFS fitting results of Pd foil, PdO, PdW and d-PdW.

Sample	Bond	CN	R(Å)	σ^2	ΔE_0 (eV)	R factor
Pd foil	Pd-Pd	12	2.74	0.0054	-4.4	0.0032
PdW	Pd-Pd	7.2	2.75	0.0073	-3.3	0.0040
d-PdW	Pd-Pd	7.9	2.76	0.0062	-4.5	0.0096
d-PdW(14h)	Pd-Pd	6.8	2.75	0.0065	-4.4	0.0031
d-PdW	Pd-W	1.4	2.42	0.0039	-3.7	0.0024

Table S3. The statistics of ORR mass activity, half wave potential and stability of typical Pd-based electrocatalyst in alkaline solution. (NA: not available)

Catalysts	Half wave potential ($E_{1/2}$)	Mass Activities at 0.9 V	Stability	Reference
PdW	0.96 V	5.2 A mg^{-1}	-10 mV (5000 cycles 0.1 M KOH)	This work
Pd metallene	0.947 V	2.76 A mg^{-1}	-11 mV (5000 cycles 0.1 M KOH)	Adv. Mater.[5]
PdMo	0.95 V	16.37 A mg^{-1}	nearly undecayed (15000 cycles 0.1 M KOH)	Nature[6]
$PdMnH_x$	0.951 V	1.08 A mg^{-1}_{Pd}	-5 mV (10000 cycles 0.1 M KOH)	Nat. Commun.[7]
PdH_x@Pt	0.933 V	7.36 A mg_{Pt}^{-1}	-5 mV (10000 cycles 0.1 M KOH)	Adv. Funct. Mater.[8]
$Pd_{0.60}Bi_{0.35}Au_{0.05}$	0.946 V	6.4 A mg_{Pd}^{-1}	-6 mV (5000 cycles 0.1 M KOH)	Nano Research[3]
Pd_5Bi_2/C	0.93 V	2.05 A mg_{Pd}^{-1}	-6 mV (5000 cycles 0.1 M KOH)	J. Am. Chem. Soc.[9]
PdAuCu	0.95 V	1.781 A mg_{Pd}^{-1}	NA	Nano Energy[10]
$Pd_{0.30}$@Ag	0.868 V	0.586 A mg_{Pd}^{-1}	-12 mV (30000 cycles 0.1 M KOH)	Adv. Sci.[11]
$PdPbH_x$	0.95 V	1.36 A mg_{Pd}^{-1}	-8 mV (50000 cycles 0.1 M KOH)	Nat. Commun.[12]
Pd_6Ni/C	0.89 V	0.22 A mg^{-1}	nearly undecayed (10000 cycles 0.1M KOH)	Sci. Adv.[13]
Pd-P (9)	0.85 V	2.21 A mg^{-1} at 0.85 V vs. RHE	NA	J. Am. Chem. Soc.[14]
o-Pd_2Sn/C	0.893 V	2.5 A mg^{-1}	-2 mV (10000 cycles 0.1 M KOH)	J. Mater. Chem. A[15]
2D PdMo metallene	0.94 V	0.92 mA μg^{-1}_{metal}	-4 mV (5000 cycles 0.1 M KOH)	Adv. Mater[16]
PdZn BMene	1.05	1.11 mA μg^{-1}_{metal}	nearly undecayed (30000 cycles 0.1M KOH)	Appl. Catal. B: Environ.[17]
Pd_3Pb UPINs/C	0.91	0.59 mA μg^{-1}_{metal}	nearly undecayed (10000 cycles 0.1M KOH)	Angew. Chem., Int. Ed.[18]
Fe-Pd UPM	0.91	0.74 mA μg^{-1}_{metal}	nearly undecayed (10000 cycles	ACS Nano[19]

			0.1M KOH)	
Pd@CS/CNF-800	0.917	0.82 mA μg^{-1}_{metal}	-4 mV (10000 cycles 0.1 M KOH)	J. Mater. Chem. A[20]
Os@Pd	0.93	0.621 mA μg^{-1}_{metal}	-1 mV (10000 cycles 0.1 M KOH)	ACS Nano[21]
$Pd_{55}Au_{45}$	0.93	0.96 mA μg^{-1}_{metal}	-15 mV (10000 cycles 0.1 M KOH)	Energy Environ. Sci.[22]
$Pd_{17}Se_{15}$ NPs/C	0.89	0.206 mA μg^{-1}_{metal}	nearly undecayed (10000 cycles 0.1M KOH)	Adv. Funct. Mater.[23]

References

[1] L. Shi, Q. Wang, Q. Ren, Q. Yang, D. Zhao, Y. Feng, H. Chen, and Y. Wang, Facile Synthesis of Pd and PdPtNi Trimetallic Nanosheets as Enhanced Oxygen Reduction Electrocatalysts. *Small*. **2022**, *18*, 2103665.

[2] G. Kresse J. Furthmüller, Efficiency of ab-initio total energy calculations for metals and semiconductors using a plane-wave basis set. *Comput. Mater. Sci.* **1996**, *6*, 15-50.

[3] X. Li, K. X. Yao, F. Zhao, X. Yang, J. Li, Y. Li, and Q. Yuan, Interface-rich Au-doped PdBi alloy nanochains as multifunctional oxygen reduction catalysts boost the power density and durability of a direct methanol fuel cell device. *Nano Res.* **2022**, *15*, 6036-6044.

[4] L. Yan, L. Xie, X.-L. Wu, M. Qian, J. Chen, Y. Zhong, and Y. Hu, Precise regulation of pyrrole-type single-atom Mn-N_4 sites for superior pH-universal oxygen reduction. *Carbon Energy*. **2021**, *3*, 856-865.

[5] F. Lin, F. Lv, Q. Zhang, H. Luo, K. Wang, J. Zhou, W. Zhang, W. Zhang, D. Wang, L. Gu, and S. Guo, Local Coordination Regulation through Tuning Atomic-Scale Cavities of Pd Metallene toward Efficient Oxygen Reduction Electrocatalysis. *Adv. Mater.* **2022**, *34*, 2202084.

[6] M. Luo, Z. Zhao, Y. Zhang, Y. Sun, Y. Xing, F. Lv, Y. Yang, X. Zhang, S. Hwang, Y. Qin, J.-Y. Ma, F. Lin, D. Su, G. Lu, and S. Guo, PdMo bimetallene for oxygen reduction catalysis. *Nature*. **2019**, *574*, 81-85.

[7] Y. Qiu, D. Jiao, H. Huang, J. Wu, M. Wang, T. Gao, X. Zhao, X. Ge, W. Zhang, W. Zheng, D. J. Singh, J. Fan, and X. Cui, Locking interstitial hydrogen atoms in Pd metallenes for efficient oxygen reduction reaction. *Nat. Commun.* **2025**, *16*, 6103.

[8] Z. Feng, D. Jiao, J. Fan, Y. Qiu, X. Ge, J. Wang, X. Zhao, W. Zhang, L. Zheng, L. Zhang, Z. Yu, W. Zheng, and X. Cui, Enhancing Oxygen Reduction Reaction in PdHx@Pt Metallenes: Unveiling the Impact of Ligand Beyond Strain Effect. *Adv. Funct. Mater.* **2025**, *n/a*, 2500522.

[9] M. Zhou, J. Guo, B. Zhao, C. Li, L. Zhang, and J. Fang, Improvement of Oxygen Reduction Performance in Alkaline Media by Tuning Phase Structure of Pd–Bi Nanocatalysts. *J. Am. Chem. Soc.* **2021**, *143*, 15891-15897.

[10] G. Wang, J. Guan, L. Xiao, B. Huang, N. Wu, J. Lu, and L. Zhuang, Pd skin on AuCu intermetallic nanoparticles: A highly active electrocatalyst for oxygen reduction reaction in alkaline media. *Nano Energy*. **2016**, *29*, 268-274.

[11] Z. Li, W. Tian, K. Hu, Y. Guo, X. Tian, W. Kang, R. Li, K. Qu, L. Wang, F. Meng, H. Zhang, and

H. Li, Oxygen-Driven Reconstruction Activates Quasi-Single Pd Sites in Hollow PdAg Nanotubes for Zinc–Air and Fuel Cells. *Adv. Sci.* **2025**, *n/a*, e09329.

[12] Y. Qiu, M. Sun, J. Wu, C. Chai, S. Wang, H. Huang, X. Zhao, D. Jiao, S. Xu, D. Wang, X. Ge, W. Zhang, W. Zheng, Y. Song, J. Fan, B. Huang, and X. Cui, Boosting oxygen reduction performances in Pd-based metallenes by co-confining interstitial H and p-block single atoms. *Nat. Commun.* **2025**, *16*, 5262.

[13] Y. Feng, Q. Shao, Y. Ji, X. Cui, Y. Li, X. Zhu, and X. Huang, Surface-modulated palladium-nickel icosahedra as high-performance non-platinum oxygen reduction electrocatalysts. *Sci. Adv. 4*, eaap8817.

[14] K. C. Poon, D. C. L. Tan, T. D. T. Vo, B. Khezri, H. Su, R. D. Webster, and H. Sato, Newly Developed Stepwise Electroless Deposition Enables a Remarkably Facile Synthesis of Highly Active and Stable Amorphous Pd Nanoparticle Electrocatalysts for Oxygen Reduction Reaction. *J. Am. Chem. Soc.* **2014**, *136*, 5217-5220.

[15] J. Liang, S. Li, Y. Chen, X. Liu, T. Wang, J. Han, S. Jiao, R. Cao, and Q. Li, Ultrathin and defect-rich intermetallic Pd_2Sn nanosheets for efficient oxygen reduction electrocatalysis. *J. Mater. Chem. A*. **2020**, *8*, 15665-15669.

[16] S. Liu, H. Teng, K. Ma, W. Miao, X. Zhou, X. Cui, X. Zhou, L. Jiang, and B. Yu Xia, Coupling Tensile Strain and Electronic Modulation in Mesoporous PdMo Metallene Nanoveins for Improved Oxygen Reduction. *Advanced Materials*. **2025**, *37*, 2508055.

[17] H. Zhang, X. Li, Y. Wang, K. Deng, H. Yu, Y. Xu, H. Wang, Z. Wang, and L. Wang, Porous PdZn bimetallene for oxygen reduction electrolysis. *Applied Catalysis B: Environmental*. **2023**, *338*, 123006.

[18] J. Guo, L. Gao, X. Tan, Y. Yuan, J. Kim, Y. Wang, H. Wang, Y.-J. Zeng, S.-I. Choi, S. C. Smith, and H. Huang, Template-Directed Rapid Synthesis of Pd-Based Ultrathin Porous Intermetallic Nanosheets for Efficient Oxygen Reduction. *Angewandte Chemie International Edition*. **2021**, *60*, 10942-10949.

[19] S. Huang, S. Lu, S. Gong, Q. Zhang, F. Duan, H. Zhu, H. Gu, W. Dong, and M. Du, Sublayer Stable Fe Dopant in Porous Pd Metallene Boosts Oxygen Reduction Reaction. *ACS Nano*. **2022**, *16*, 522-532.

[20] H. E. Bae, J. E. Park, T. B. N. Huynh, J. Song, S. K. Cho, Y.-E. Sung, Y.-H. Cho, and O. J. Kwon, A high-durability palladium catalyst for the oxygen reduction reaction in an alkaline environment. *Journal of Materials Chemistry A*. **2024**, *12*, 31467-31479.

[21] P. Prabhu, V.-H. Do, T. Yoshida, Y. Zhou, H. Ariga-Miwa, T. Kaneko, T. Uruga, Y. Iwasawa, and J.-M. Lee, Subnanometric Osmium Clusters Confined on Palladium Metallenes for Enhanced Hydrogen Evolution and Oxygen Reduction Catalysis. *ACS Nano*. **2024**, *18*, 9942-9957.

[22] S. Qiao, H. Shou, W. Xu, Y. Cao, Y. Zhou, Z. Wang, X. Wu, Q. He, and L. Song, Regulating and identifying the structures of PdAu alloys with splendid oxygen reduction activity for rechargeable zinc–air batteries. *Energy & Environmental Science*. **2023**, *16*, 5842-5851.

[23] Z. Hu, L. Huang, M. Ma, L. Xu, H. Liu, W. Xu, and J. Yang, A Quick Joule-Heating Coupled with Solid-Phase Synthesis for Carbon-Supported Pd–Se Nanoparticles Toward High-Efficiency Electrocatalysis. *Advanced Functional Materials*. **2024**, *34*, 2405945.